JACS JOURNAL OF THE AMERICAN CHEMICAL SOCIETY

pubs.acs.org/JACS Article

# Two-Dimensional Violet Phosphorus $P_{11}$: A Large Band Gap Phosphorus Allotrope

Gary Cicirello,[#] Mengjing Wang,[#] Quynh P. Sam, James L. Hart, Natalie L. Williams, Huabing Yin,* Judy J. Cha,* and Jian Wang*

Cite This: J. Am. Chem. Soc. 2023, 145, 8218–8230 Read Online





**ABSTRACT:** The discovery of novel large band gap two-dimensional (2D) materials with good stability and high carrier mobility will innovate the next generation of electronics and optoelectronics. A new allotrope of 2D violet phosphorus $P_{11}$ was synthesized via a salt flux method in the presence of bismuth. Millimeter-sized crystals of violet-$P_{11}$ were collected after removing the salt flux with DI water. From single-crystal X-ray diffraction, the crystal structure of violet-$P_{11}$ was determined to be in the monoclinic space group $C2/c$ (no. 15) with unit cell parameters of $a$ = 9.166(6) Å, $b$ = 9.121(6) Å, $c$ = 21.803(14)Å, $\beta$ = 97.638(17)°, and a unit cell volume of 1807(2) Å$^3$. The structure differences between violet-$P_{11}$, violet-$P_{21}$, and fibrous-$P_{21}$ are discussed. The violet-$P_{11}$ crystals can be mechanically exfoliated down to a few layers (~6 nm). Photoluminescence and Raman measurements reveal the thickness-dependent nature of violet-$P_{11}$, and exfoliated violet-$P_{11}$ flakes were stable in ambient air for at least 1 h, exhibiting moderate ambient stability. The bulk violet-$P_{11}$ crystals exhibit excellent stability, being stable in ambient air for many days. The optical band gap of violet-$P_{11}$ bulk crystals is 2.0(1) eV measured by UV−Vis and electron energy-loss spectroscopy measurements, in agreement with density functional theory calculations which predict that violet-$P_{11}$ is a direct band gap semiconductor with band gaps of 1.8 and 1.9 eV for bulk and monolayer, respectively, and with a high carrier mobility. This band gap is the largest among the known single-element 2D layered bulk crystals and thus attractive for various optoelectronic devices.

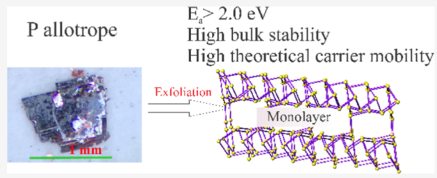


## ■ INTRODUCTION

Driven by application needs in next-generation electronics and optoelectronics, extensive efforts have been dedicated to studying and discovering wide band gap two-dimensional (2D) layered materials with band gaps >2 eV.[1−16] 2D layered materials can be catalogued into two groups: elemental and compound 2D materials.[17−22] The elemental 2D materials, composed of single elements and simple bonding structures, may be more suitable for device applications compared to compound 2D materials.[17−22] The largest band gap of elemental 2D materials is in the single-layered black phosphorus with a band gap of ~2.3 eV;[23−25] however, applications of single-layered black phosphorus are impeded by its low ambient stability.[26−34] Exploring new elemental 2D compounds with band gap ≥2.0 eV, high stability, and high mobility is thus essential for developing next-generation electronics and optoelectronics.

The allotropes of phosphorus remain exciting for decades due to the continual discovery of new 2D materials.[35−52] Experiments and theory calculations continue to discover and predict more 2D materials.[35−52] In this work, a new phosphorus allotrope violet-$P_{11}$ was grown as large crystals by a novel method that combines high-temperature salt flux and bismuth metal. The newly discovered layered violet phosphorus $P_{11}$ has a band gap of 2.0(1) eV for bulk crystals, coupled with good bulk stability and high predicted electron mobility (1307.32 cm$^2$ V$^{-1}$ s$^{-1}$). The crystal structure of violet-$P_{11}$ was determined by a combination of synchrotron powder X-ray diffraction (PXRD), single-crystal XRD, and scanning transmission electron microscopy (STEM). The crystal structure differences between the known allotropes of phosphorus, violet-$P_{11}$, violet-$P_{21}$, and fibrous-$P_{21}$, are discussed. Very thin, few-layered violet-$P_{11}$ crystals were obtained by mechanical exfoliation and found to be stable upon exposure to air for at least 1 h. The bulk violet-$P_{11}$ crystals exhibit excellent stability, being stable in ambient air for many days. The thickness-dependent characteristics of violet-$P_{11}$ crystals were revealed by the photoluminescence (PL) and Raman measurements. Density functional theory (DFT) calculations were employed to study the electronic structures of violet-$P_{11}$ crystals. The excellent bulk air stability, easy growth of large crystals, and high predicted carrier mobility coupled with its large band gap of violet-$P_{11}$ compared with black phosphorus make violet-$P_{11}$ a potential candidate for future optoelectronic applications.

**Received:** February 16, 2023
**Published:** March 30, 2023

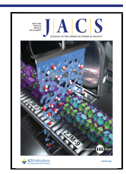





https://doi.org/10.1021/jacs.3c01766
J. Am. Chem. Soc. 2023, 145, 8218–8230

## ■ EXPERIMENTAL DETAILS

**Synthesis and Crystal Growth.** Starting materials were handled in an argon-filled glovebox with $O_2$ levels below 1 ppm. All starting materials were of commercial grade and used without further purification: Bi pieces (Alfa Aesar, 99.99%), red P powder (Alfa Aesar, 99+%), NaCl (Alfa Aesar, 99.9%), KCl (Sigma, 99.5%), and $AlCl_3$ (Alfa Aesar, 99.9%). Red crystals of violet-$P_{11}$ were grown in the salt flux $AlCl_3$/KCl/NaCl (molar ratio of 0.601/0.141/0.258), which melts around 386 K. A total of 0.5 g of Bi/P molar ratio = 1:1 elements were mixed with 0.5 g salt flux. The mixtures were sealed into carbonized silica tubes. The sealed quartz tubes were heated from room temperature to 773 K within 1/2 h, annealed at this temperature for 120 h, and then the furnace was shut off. The salt flux was removed by DI water. The crystals show a red color with a significant layered nature, as shown in Figure 1a. The Bi elements seem to act as catalysts during the crystal growth process. No crystals were found in the reaction when Bi was absent. Increasing the total mass of raw materials and flux and putting them in a larger quartz tube can result in higher yields. The synthesis yield can also be increased by heating reaction vessels twice using the same temperature profile. The elemental analysis using energy-dispersive X-ray (EDX) spectroscopy confirmed the absence of Bi elements in violet-$P_{11}$ crystals (Table S1).

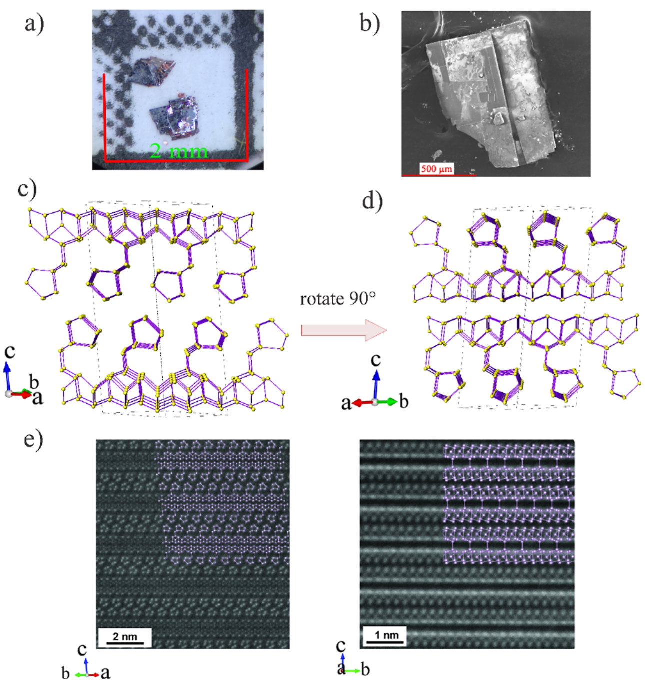


Figure 1. (a) Optical micrograph of violet-$P_{11}$ crystals; (b) SEM image of a violet-$P_{11}$ crystal; (c,d) crystal structure of violet-$P_{11}$ viewed along two directions; and (e) high-angle annular dark field (HAADF) STEM image of a violet-$P_{11}$ crystal viewed along two directions with scale bars of 2 nm (e left) and 1 nm (e right).

**Characterizations.** *Single-Crystal XRD.* The crystal data were collected on a Bruker SMART APEX-II diffractometer equipped with a CCD area detector and graphite-monochromated Mo K$\alpha$ radiation ($\lambda$ = 0.71073 Å) under a nitrogen gas atmosphere at 100 K. Crystallographic data for violet-$P_{11}$ have been deposited to the Cambridge Crystallographic Data Centre, CCDC, 12 Union Road, Cambridge CB21EZ, UK. Copies of the data can be obtained free of charge by quoting the depository numbers CCDC-2208167.

*Powder X-ray Diffraction, Scanning Electron Microscopy, and Energy-Dispersive X-ray Spectroscopy Analysis.* Lab PXRD analysis was performed at room temperature using a Rigaku Miniflex VI diffractometer employing Cu K$\alpha$ radiation. High-resolution PXRD experiments were carried out at the 11bm beamline at the Advanced Photon Source at Argonne National Laboratory. Amorphous $SiO_2$ was mixed with violet-$P_{11}$ to reduce its layered orientation during the PXRD measurement. Elemental analysis was carried out on a Hitachi S4100T scanning electron microscope with EDX microanalysis (Oxford INCA Energy).

**UV−Vis Measurements.** Diffuse-reflectance spectra were collected at room temperature by a PERSEE-T8DCS UV−Vis spectrophotometer equipped with an integration sphere in the wavelength range of 230−850 nm.

**Scanning Transmission Electron Microscopy.** Bulk crystals were mechanically exfoliated into few-layered samples using Scotch tape and transferred to $SiO_2$/Si substrates. STEM samples were prepared using a focused ion beam (Thermo Fisher Scientific Helios) and the standard lift-out procedure. Final thinning was performed with 5 kV Ga ions. STEM images were taken on a Thermo Fisher Scientific Spectra 300 TEM at 300 kV. Simulated STEM images were generated using Computem.

**Electron Energy-Loss Spectroscopy Measurements.** Low-loss electron energy-loss spectroscopy (EELS) measurements to determine the band gap were performed on a monochromated, aberration-corrected TFS Titan Themis 300 X-FEG, with a Gatan GIF Tridiem energy filter. The measurements were performed with an accelerating voltage of 60 kV, a probe convergence semiangle of 60 mrad, and an EELS collection semiangle of 40 mrad. From vacuum zero-loss peak (ZLP) measurements, the ZLP full width at half-maximum (fwhm), full width at tenth-maximum, and full width at a hundredth-maximum were 0.22, 0.45, and 0.90 eV, respectively. Measurements were performed on an exfoliated flake and transferred to a SiN STEM grid using a PDMS stamp. The presented EELS measurements all come from the same flake, which exhibited a thickness gradient in the studied region, ranging from 0.2 to 0.69 inelastic mean free paths. Using ∼45 nm as the inelastic mean free path for phosphorus at 60 kV, the thickness ranged from 9 to 31 nm (vide infra).

**Photoluminescence.** PL measurements of exfoliated flakes were carried out using a HORIBA LabRAM HR Evolution under an excitation of 532 nm with a power of 1 mW and collected by a Synapse spectrometer with a grating of 600 grooves/mm under ambient conditions.

**Raman Spectroscopy.** Raman spectra of exfoliated flakes were collected with a HORIBA LabRAM HR Evolution system under an excitation of 633 nm at 1 mW and collected by a spectrometer with a grating of 1800 grooves/mm under ambient conditions.

**Atomic Force Microscopy.** Height profiles of few-layered exfoliated crystals were obtained using a Cypher ES microscope from Asylum Research. Atomic force microscopy (AFM) images and three-dimensional (3D) renderings of few-layered exfoliated crystals were acquired using a Veeco Icon Atomic Force Microscope in tapping mode using a NanoWorld Arrow NC AFM probe at a scan rate of 2 Hz at 256 pixels/line. All images were performed under ambient conditions.

**Device Fabrication.** Few-layered flakes transferred on the $SiO_2$/Si wafers were spin coated with layers of ebeam-resist and written with electron beam lithography (Nabity NPGS, Helios G4 FIB-SEM) at a voltage of 30 kV and a current of 1.6 nA. The written pattern was etched with argon plasma at 50 mW for 10 min and in situ deposited with 15 nm Cr and 200 nm of Au using a ultrahigh vacuum electron beam evaporator.

**Field-Effect Transistor Measurements and Mobility Calculation.** Back-gated field-effect transistor (FET) transfer curves of the devices were measured in air using the Agilent Technologies B1500A semiconductor device analyzer. The carrier mobility was calculated based on the transfer curve of the device using the equation: $= \frac{\left(\frac{\partial I_D}{\partial V_{GS}}\right) L}{V_{DS} C_{ox} W}$, where $\left(\frac{\partial I_D}{\partial V_{GS}}\right)$ is the maximum transconductance and $C_{ox}$ is the gate capacitance of 285 nm thick $SiO_2$ with a value of $1.2 \times 10^{-8}$ F/cm$^2$; $L$ and $W$ are the length and width of the conducting channel, respectively.


https://doi.org/10.1021/jacs.3c01766
J. Am. Chem. Soc. 2023, 145, 8218−8230

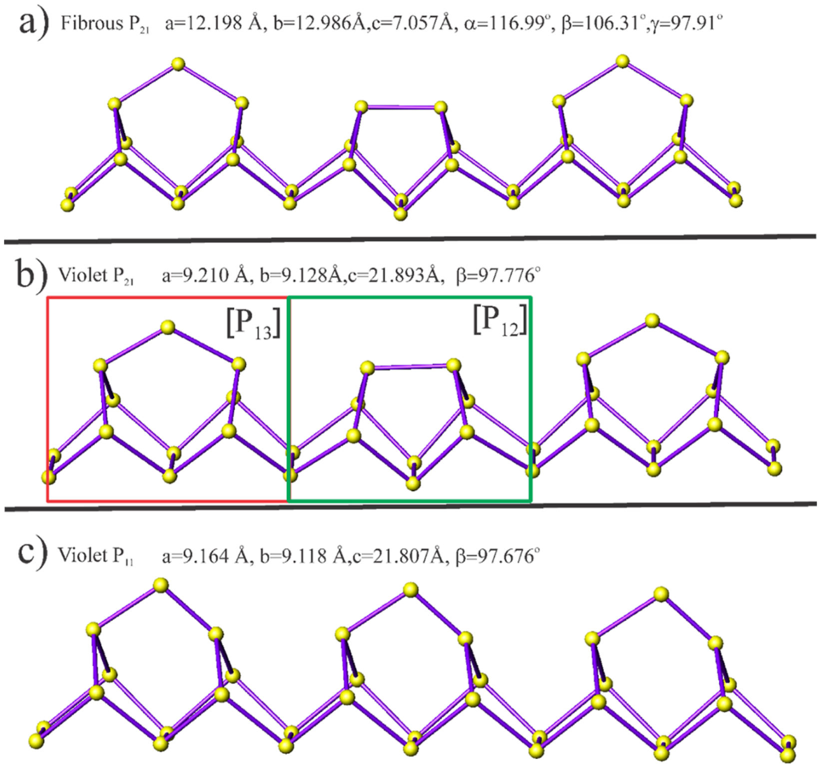


**Figure 2.** Detailed views of 1D structural fragment $[P_5]$ chain of (a) fibrous $P_{21}$;[35] (b) violet $P_{21}$;[52] and (c) this work's violet-$P_{11}$. P atoms are presented in yellow color; P−P bonds are presented by purple sticks. The $[P_{13}]$ units and $[P_{12}]$ units are highlighted by red and green squares, respectively.

**DFT Calculations.** The first-principles calculations were performed within the framework of DFT using the Vienna Ab initio Simulation Package (VASP) code.[53−55] Generalized gradient approximation within the Perdew−Burke−Ernzerhof (PBE) method was employed to describe exchange−correlation potential.[56] A plane-wave basis set along with an energy cutoff of 500 eV was used to describe electron wavefunctions. The interactions between electrons and nuclei were described within the projector-augmented wave method.[55] The Brillouin zone was sampled using the mesh sizes of 5 × 5 × 1 for 2D systems and 4 × 4 × 2 for 3D bulk in the Γ-centered Monkhorst−Pack scheme.[57] The convergence criteria for electronic and ionic relaxations were set as $10^{-6}$ eV and 0.01 eV/Å, respectively. Moreover, a 20 Å vacuum space along the *z*-direction was added to model the characteristics of 2D monolayers. Particularly, the DFT-D3 method was employed to describe the van der Waals interactions.[58] Electronic band structures were also obtained by the Heyd−Scuseria−Ernzerhof (HSE06) screened hybrid functional.[59] The phonon spectrum was calculated using the finite displacement method within a 3 × 3 × 1 supercell as implemented in the PHONOPY package.[60] Ab initio molecular dynamics (AIMD) simulations are performed on a 2 × 2 × 1 supercell within the canonical ensemble (*NVT*) using a Nosé−Hoover thermostat.[61,62]

**Carrier Mobility Calculations.** In 2D monolayers, the carrier mobility is calculated by the deformation potential (DP) theory,[63] which is described as $\mu = \frac{e\hbar^3 C_{2D}}{k_B T m^* m_d E_1^{\,2}}$, where $\hbar$, $k_B$, and $T$ represent Planck's constant divided by $2\pi$, Boltzmann constant, and temperature, respectively.[64−66] The term $C_{2D}$ is the elastic modulus of a uniformly deformed 2D crystal. $m^*$ is the effective mass of the carrier in the transport direction defined as $m^* = \pm\hbar^2\left(\frac{d^2E_k}{dk^2}\right)^{-1}$, where $k$ is the wave vector, $E_k$ is the energy related to the wave vector $k$; and $m_d$ is the average effective mass determined by $m_d = \sqrt{m_x^* m_y^*}$. The term $E_1$ represents the DP composed of the conduction band minimum (CBM) for electrons and valence band maximum (VBM) for holes, as determined by $E_1 = \Delta E_i/(\Delta l/l_0)$, where $\Delta E_i$ is the energy shift of the band edge of CBM or VBM vs. the lattice deformation $\Delta l/l_0$. These data are calculated with strains varied from −0.01 to 0.01 in a step of 0.005. All the mobilities have been calculated at 300 K.

## ■ RESULTS AND DISCUSSION

**Crystal Growth and Crystal Structure.** The millimeter-sized crystals of violet-$P_{11}$ were grown in a salt flux and are shown in Figure 1a. The bulk violet-$P_{11}$ crystals exhibit extraordinarily high ambient stability (vide infra). After water treatments, there were no detectable changes found on the crystals, which were verified by scanning electron microscopy (SEM) and STEM (Figure 1b, Table S1, and Figure S1) and PXRD (Figure S2). Single-crystal XRD revealed that violet-$P_{11}$ crystallizes in the monoclinic space group *C*2/*c* (no. 15) with unit cell parameters of $a$ = 9.166(6) Å, $b$ = 9.121(6) Å, $c$ = 21.803(14)Å, $\beta$ = 97.638(17)°, and a unit cell volume of 1807(2) Å$^3$. The Wyckoff sequence of violet-$P_{11}$ is $g^{11}$ with Pearson symbol *oP*72. The crystal structure of violet-$P_{11}$ viewed along two different directions is presented in Figure 1c,d. The selected crystal data and structure refinement parameters for violet-$P_{11}$ are presented in Table S2. The refined atomic coordinates and selected important interatomic distances of violet-$P_{11}$ are summarized in Tables S3 and S4, respectively.

There are 11 distinct P atoms in the asymmetric unit cell of violet-$P_{11}$ with full occupancy. The violet-$P_{11}$ structure is constructed by 2D $[P_{11}]$ slabs. The 2D $[P_{11}]$ slabs are made by two one-dimensional (1D) $[P_5]$ chains that are perpendicular to each other and linked by the bridging P atoms. The crystal structure of violet-$P_{11}$ determined from single-crystal XRD is also supported by STEM images (Figure 1e) and property

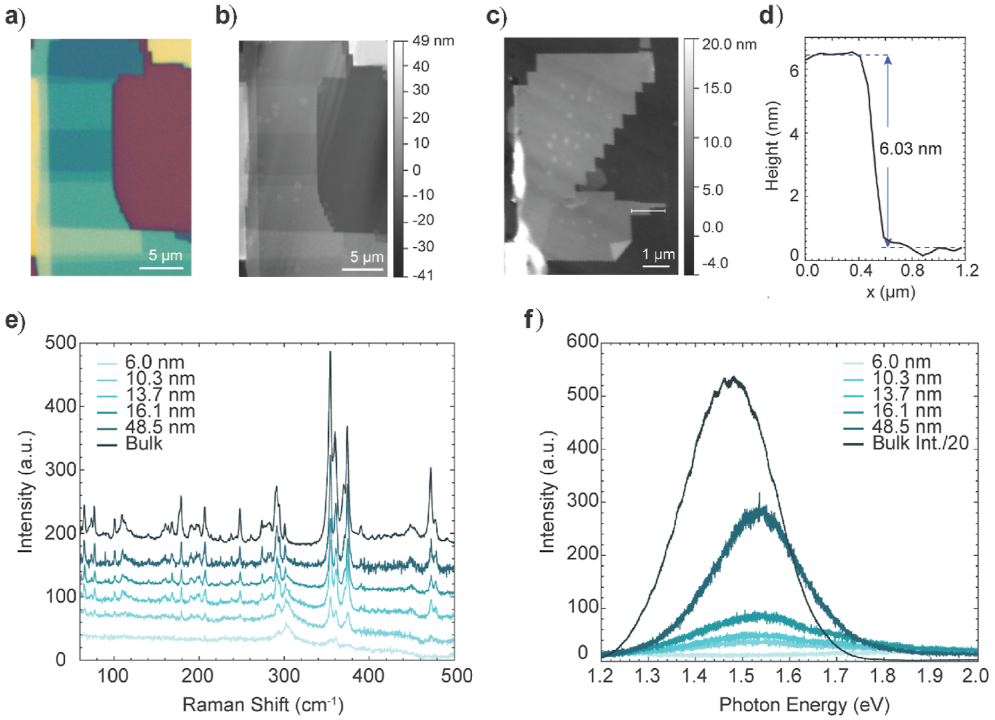


**Figure 3.** Thickness-dependent Raman and PL emission spectra of violet-$P_{11}$. (a,b) Optical micrograph (a) and AFM height map (b) of a multilayered exfoliated flake. (c) AFM height map of a thin violet-$P_{11}$ flake. (d) Height trace of the flake along the marked white solid line in (c). (e) Thickness-dependent Raman spectra of violet-$P_{11}$ from trilayer to bulk under the excitation of a 633 nm laser. (f) Thickness-dependent PL emission spectra of violet-$P_{11}$ from trilayer to bulk under the excitation of a 532 nm laser.

measurements (vide infra). The detailed view of the 1D [$P_5$] chain is shown in Figure 2c. The 1D [$P_5$] chain is made of interconnected $P_5$ pentagon rings sharing three P atoms. A similar connectivity of $P_5$ pentagon rings was also discovered in $La_7Zn_2P_{11}$,[67] black P,[68] violet-$P_{21}$,[52] and fibrous-$P_{21}$.[35] The covalent radius for P is 1.07 Å. The P−P distances in violet-$P_{11}$ fall into the range of 1.95(2) Å-2.266(12) Å (Table S4), which is typical for homoatomic P−P bond distances such as in black P (2.224 Å),[68] violet-$P_{21}$ (2.186−2.285 Å),[52] fibrous-$P_{21}$ (2.178−2.299 Å),[35] $La_2Ba_6Cu_{16}P_{30}$ (2.071−2.428 Å),[69] $K_2BaP_2S_6$ (2.223(4) Å),[70] $Ba_8Cu_{16}P_{30}$ (2.159−2.299 Å),[71] $La_7Zn_2P_{11}$ (2.207(7) Å),[67] $La_4Zn_7P_{10}$ (2.151(8) Å),[72] and so forth.

At first glance, the structure of violet-$P_{11}$ is similar to the known fibrous-$P_{21}$ and violet-$P_{21}$. The structure comparison of the three phosphorus allotropes is shown in Figure S3, and a detailed analysis verifies the structure differences among the three phosphorus allotropes. The fibrous-$P_{21}$ is constructed by isolated [$P_{21}$] chains, while violet-$P_{21}$ and violet-$P_{11}$ are built by 2D phosphorus layers. The unitcell parameters of violet-$P_{11}$ are close to those of violet-$P_{21}$ (Figure 2). However, the structure symmetry of violet-$P_{11}$ [$C2/c$ (no. 15)] is higher than that of violet-$P_{21}$ [$P2/n$ (no. 13)]. There are 21 distinct P atoms in the asymmetric unitcell of violet-$P_{21}$ with full occupancy, while violet-$P_{11}$ has only 11 distinct P atoms in its asymmetric unitcell. All three allotropes are made by [$P_5$] 1D chains. The detailed view of [$P_5$] 1D chains of the three phosphorus allotropes is shown in Figure 2. As we can see, violet-$P_{21}$ has a [$P_5$] 1D chain identical to fibrous-$P_{21}$. The [$P_5$] 1D chain in violet-$P_{21}$ and fibrous-$P_{21}$ is alternatively linked by [$P_{13}$] units and [$P_{12}$] units. The [$P_{13}$] units are constructed by four $P_5$ pentagon rings with two pentagon rings linked by a bridging P atom. The bridging P atoms also connect two neighboring [$P_5$] chains to form 2D layers in the violet-$P_{21}$ or 1D chains in the fibrous-$P_{21}$. The [$P_{12}$] units are built by four $P_5$ pentagon rings with two pentagon rings linked by two vertex P atoms. In violet-$P_{11}$, there are only [$P_{13}$] units repeatedly interconnected through the crystal structure (Figure 2c). Moreover, the PXRD (Figure S2), cross-sectional STEM data analysis (Figure S4), Raman spectroscopy measurements, DFT calculations, and UV−Vis spectrum measurements all confirmed the structure difference between the violet-$P_{21}$ and the violet-$P_{11}$ (Table S5 and vide infra.)

**Layer-Dependent Optical Properties.** Guided by the "2D" layered nature of the violet-$P_{11}$, we mechanically exfoliated the bulk millimeter-sized crystals down to multilayered micrometer-sized flakes, as displayed in Figure 3a,b. These exfoliated flakes have thicknesses ranging from 10 to 50 nm, differing in their color and optical contrast. The thinnest flake we achieved has a thickness of 6.0 nm, corresponding to three units of violet-$P_{11}$ stacking slabs (Figure 3c,d). We note that the exfoliated flakes shown in Figure 3a,c possess indented edges with an angle of 90°, reflecting the monoclinic nature of the violet-$P_{11}$ crystals.

As the flake thickness is reduced with exfoliation, optical properties like Raman spectra and PL exhibit strong thickness-dependent characteristics, as shown in Figure 3e,f, respectively. We measured the Raman spectra of the bulk crystal and exfoliated flakes down to a trilayer flake. Due to the large number of phosphorus atoms inside a violet-$P_{11}$ unit cell, the number of active Raman modes is large. To simplify the discussion, we will divide the Raman modes into two groups (groups I and II), as referred in the Raman investigations on Hittorf's red phosphorus flake and amorphous red phosphorus.[73] Group I includes Raman modes from 50 to 140 $cm^{-1}$, where interlayer vibration modes are populated due to their


https://doi.org/10.1021/jacs.3c01766
J. Am. Chem. Soc. 2023, 145, 8218−8230

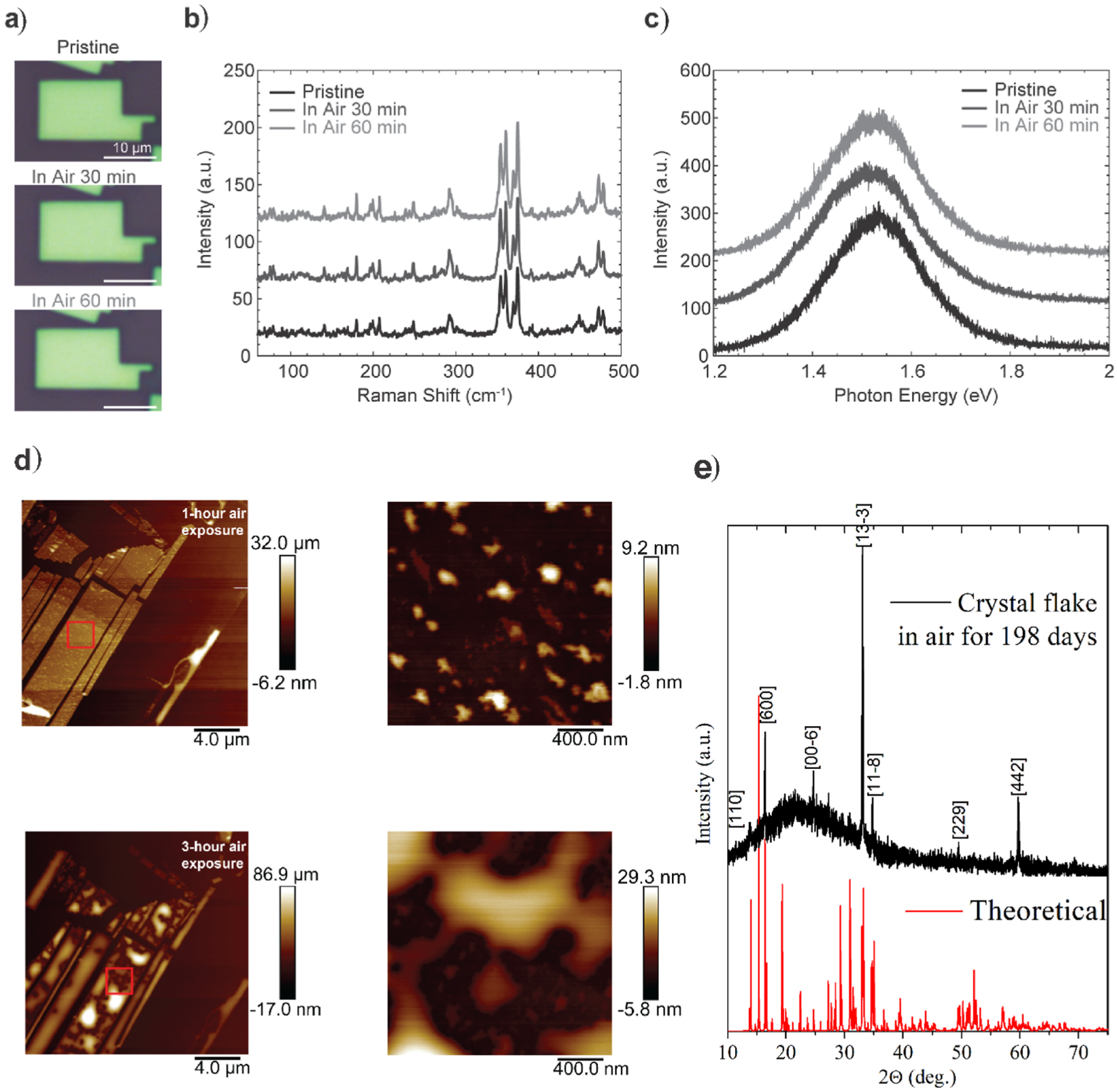


**Figure 4.** Optical images (a), Raman spectra (b), and PL spectra (c) of an exfoliated violet-$P_{11}$ flake as a function of air exposure time, spanning the freshly exfoliated pristine state, in air for 30 min and in air for 60 min. (d) AFM height map of thin violet-$P_{11}$ flakes after 1 h (top left) and 3 h (bottom left) of air exposure; (right images) enlarged images of the regions shown by the red squares in top left and bottom left, respectively. (e) PXRD results of a crystal flake (1.1 mm × 1.1 mm × 0.5 mm) stored in ambient air for 198 days.

large masses and small restoring forces. Group II contains the modes from 140 to 500 $cm^{-1}$ where most modes belong to the intralayer bending and stretching modes. These two groups of Raman modes exhibit distinct thickness-dependent characteristics. (1) The intensities of the group-I modes gradually die down from the bulk to the trilayer sample, indicating a significant reduction of interlayer vibrations as the flake thickness decreases, particularly in the case of the trilayer sample where no active interlayer vibration modes are present; (2) however, most intralayer vibration modes in group II are present regardless of the flake thinning down. For example, modes populated around 280−400 $cm^{-1}$ remain active even in the trilayer sample, accompanied by a noticeable peak broadening due to a reduced crystallite size.

PL, a radiative combination of photo-generated electrons and holes in semiconductors, typically reflects the nature of the electron band structure as well as the energy state of the defects. We measured the PL emission spectra of the violet-$P_{11}$ crystal as a function of flake thickness under the excitation of a 532 nm (2.33 eV) laser at room temperature, as summarized in Figure 3f. The bulk violet-$P_{11}$ crystal has a strong and broad PL response centered around 1.47 eV with an fwhm of 0.23 eV. This broad peak width strongly suggests the PL of the bulk at room temperature to be a defect-dominated emission rather than a near-edge band emission. The very broad fwhm of violet-$P_{11}$ crystals may originate from the defects,[74,75] which was also observed in black-P[76] and violet-$P_{21}$.[52] The weak signals of PL for thin violet-$P_{11}$ flakes might be due to its air instability (vide infra). Carrying out PL experiments under vacuum and cryogenic PL measurements is essential and ongoing to better understand the properties of violet-$P_{11}$ crystals. As the flake thickness decreases to 6.0 nm, the PL at 1.47 eV of the bulk sample undergoes a considerable intensity reduction as well as a redshift to a new center at 1.55 eV. Concurrently, a new shoulder peak centered around 1.70 eV emerges in samples with thicknesses less than 16 nm. At a


https://doi.org/10.1021/jacs.3c01766
J. Am. Chem. Soc. 2023, 145, 8218−8230

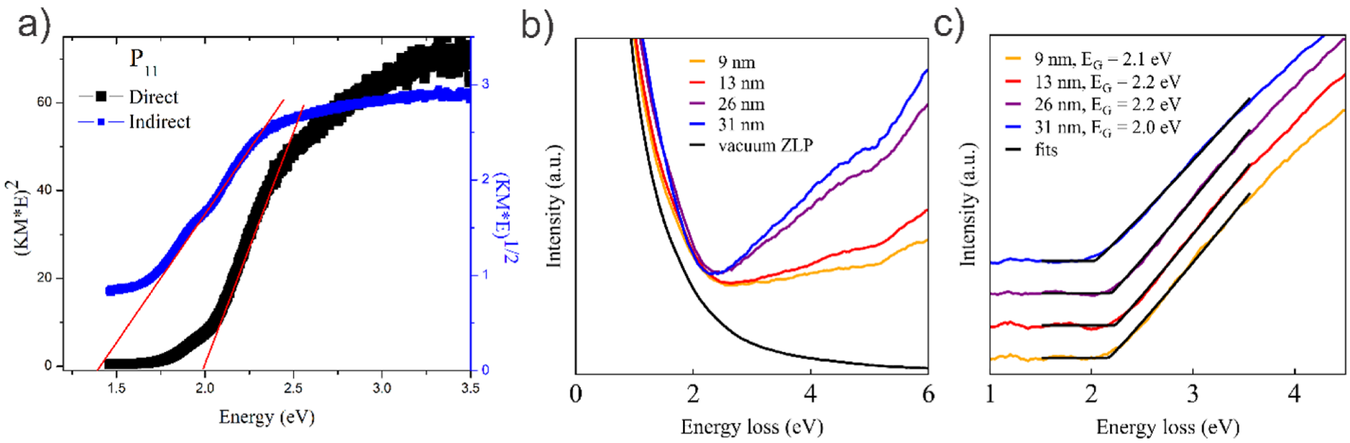


**Figure 5.** (a) Band gap estimation of violet-$P_{11}$ bulk crystals via UV−Vis spectroscopy. (b) Raw EELS data from violet-$P_{11}$ of various thicknesses, as well as the vacuum ZLP for reference. All data are scaled vertically based on the ZLP maximum. (c) Background-subtracted EELS data, shifted vertically for clarity. Each spectrum is fit independently. The fits are shown in black, and the fitted parameters are listed in the legend.

flake thickness of 6.0 nm, only a broad peak centered around 2.0 eV is observable with a signal-to-noise ratio of about 2.14, as shown in a rescaled plot in Figure S5. Due to a lack of time-dependent and temperature-dependent PL study within the scope of this work, we cannot identify the nature of the excitons observed in our PL emission spectra. However, this thickness-dependent PL evolution sheds some insights into the thickness-dependent electronic band structure of violet-$P_{11}$. (1) Since all violet-$P_{11}$ samples have PL response regardless of thickness, the direct band gap of violet-$P_{11}$ crystals from bulk down to 6 nm is less than the excitation laser energy at 2.33 eV. (2) There are multiple excitation states present in the gap between the conduction band and the valence band of violet-$P_{11}$ with varying quantum yields, as evidenced by the multipeak characteristics of PL in samples with a thickness from 10 to 16 nm. (3) The significant increase of PL intensity in bulk as compared to that of a few-layered sample can be attributed to either a reduction of band gap in the bulk or a switch from indirect band gap to direct band gap as the thickness increases from the nanometer to millimeter scale.

**Extraordinary Ambient Stabilities for Bulk Violet-$P_{11}$.** The stability of a nanomaterial under ambient conditions is critical to its performance for applications in electronic and optoelectronic devices. The air stability of phosphorus allotropes is challenging due to the presence of lone pairs at the surface,[76−80] which gets more pronounced in thinner flakes due to increased surface to volume ratios.[76−80] Hence, in this work, the ambient stability of bulk crystals and thin flakes of violet-$P_{11}$ were studied carefully via AFM characterization, Raman spectroscopy, optical imaging, PL spectra, SEM, TEM, TEM−EDS quantification, PXRD, and AIMD simulations as a function of air exposure time (Figures 4 and S6−S12 and Table S6). The exfoliated violet-$P_{11}$ flake exhibited a moderate stability against air exposure, in which no observable degradation was detected after exposure to air for 1 h. Thus, the violet-$P_{11}$ thin flakes are stable in ambient air within a 1 h period. As demonstrated in Figure 4a, a mechanically exfoliated flake on a $SiO_2$/Si substrate was placed in air without further treatment or protection. The color and the optical contrast of the flake remain unchanged after 1 h of air exposure. We tracked the Raman spectra of the flake throughout the 1 h of air exposure, as summarized in Figure 4b. Since Raman spectroscopy is a tool to inform the surface atomic vibration conditions, which are sensitive to the intrinsic crystal quality and extrinsic factors like strain and doping, Raman spectroscopy can probe if any significant oxidation occurs to the violet-$P_{11}$ flake, which will lead to a breaking of atomic bonds and a vanishing of the original Raman vibration modes. Strikingly, the Raman spectrum of the violet-$P_{11}$ flake collected after 1 h of air exposure is almost identical to that of the freshly exfoliated one. There is no obvious degradation of peak intensity and no emergence of new Raman modes within 1 h of air exposure. Similar air stability is found in the time-dependent PL in Figure 4c. The PL emission spectrum does not have any obvious changes in the shape, intensity, and position, as indicated in the peak fitting result summarized in Figure S6. The selected area electron diffraction also did not detect any noticeable degradation of crystallinity after 90 min of air exposure (Figure S7a−c). EELS (sensitive to bonding) analysis shows that the P $L_{2,3}$ edge does not show any obvious changes after 90 min of air exposure (Figure S7e). When exposed to ambient air longer, surface degradation did occur to thin violet-$P_{11}$ flakes. As shown in Figure 4d, the AFM imaging showed obvious surface degradation after 3 h of air exposure, which are supported by the AFM height maps (Figure S8), optical images (Figure S9), and STEM−EDS collection on a surface of a 57 nm thick violet-$P_{11}$ crystal (Figure S7d).

The mechanism of surface reactions between the violet-$P_{11}$ single layer and oxygen is an important question for understanding the degradation of violet-$P_{11}$ crystals. To explore the ambient stability of monolayer violet-$P_{11}$ under the $O_2$ environment, we performed AIMD at room temperature (300 K) for 5 ps (Figure S10). Our AIMD results manifest that the violet-$P_{11}$ single layer easily reacts with $O_2$, which is very similar to the case of black phosphorene.[79,80] After 5 ps of contact, some gaseous-phase $O_2$ molecules dissociate into O atoms on the violet-$P_{11}$ surface and form the chemisorbed oxygen in the dangling or bridge configuration, as shown in Figure S10b. As shown in Figure S10a, there is a significant decrease in total energy at 3 ps, which means the occurrence of surface oxidation. Such simulation results indicate that the interaction between violet-$P_{11}$ and $O_2$ molecules is relatively strong. Thus, some air-stable passivation layers may be necessary to encapsulate the violet-$P_{11}$ thin layers or monolayer in devices.[78]


https://doi.org/10.1021/jacs.3c01766
J. Am. Chem. Soc. 2023, 145, 8218−8230

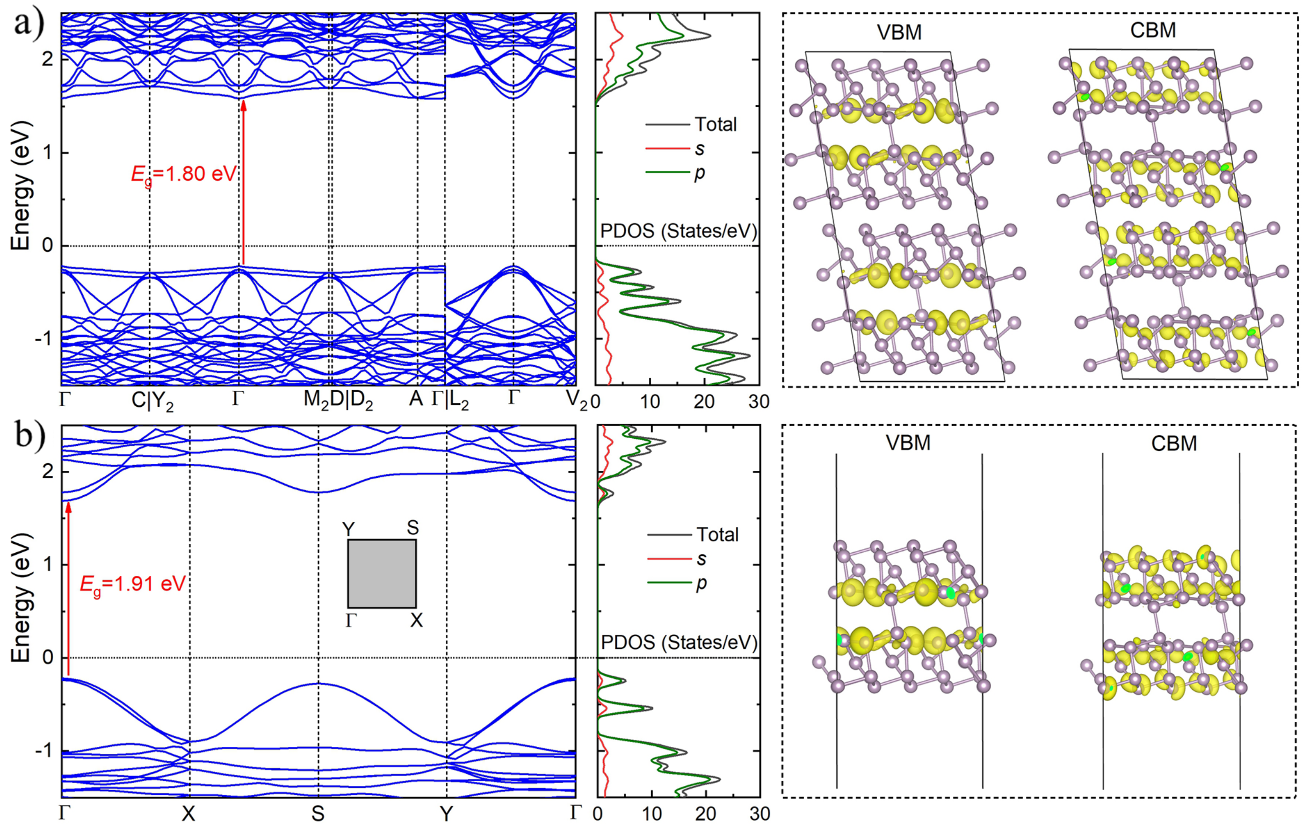


**Figure 6.** Band structures, the partial density of states, and electron density distribution at the VBM and the CBM of (a) bulk and (b) monolayer violet-$P_{11}$ based on the HSE06 functional. The Fermi level is set at 0.

The air stability increases with increasing thickness of violet-$P_{11}$ crystals. As summarized in Table S6, a 27 nm thick flake shows almost double the amount of oxygen than a 96 nm thick flake under the same air exposure. The SEM imaging of a thick and thin exfoliated violet-$P_{11}$ crystals after exposure to air for 23 days is shown in Figure S11. As shown in Figure S11, no noticeable change was found for the bulk crystals, while the thin flakes showed morphological change on the top surface. Raman spectra and optical images of a thick violet-$P_{11}$ crystal on a PDMS substrate are presented in Figure S12. Strong and characteristic Raman signals of violet-$P_{11}$ crystals were present after the sample was exposed to air for 7 days, while impurity signals did appear after exposure to air for 1 day. Another proof of the robust stability of bulk violet-$P_{11}$ is that all violet-$P_{11}$ crystals were collected after water treatment for about 30 min. A crystal flake stored in ambient air for 198 days still showed PXRD signals (Figure 4e), which indicates the presence of a crystalline phase. In conclusion, violet-$P_{11}$ bulk crystals exhibit extraordinary ambient stabilities. Thin flakes of violet-$P_{11}$ crystals can be stable in air for about 90 min.

**Linear Optical Property Measurements.** The large band gap of violet-$P_{11}$ was verified by both experimental results (Figures 5 and S13) and DFT calculation results (vide infra). The measured optical band gap of bulk violet-$P_{11}$ crystals is 2.0(1) eV for direct allowed transition (Figure 5a) since bulk violet-$P_{11}$ is predicted to be a direct band gap semiconductor (vide infra). EELS was also employed to estimate the band gap of violet-$P_{11}$ crystals (Figure 5b,c). From the raw EELS data (Figure 5b), all spectra are monotonically decreasing, with a slope similar to the vacuum reference, until a sharp feature at ~2 eV is observed. To process the data, we fit the ZLP tail with a decaying power law function from 1 to 1.8 eV. The background-subtracted spectra are shown in Figure 5c. We then fit the data using the following equation: $I \sim (E - E_G)^n$, where $I$ is the EELS intensity, $E$ is the energy, $E_G$ is the fitted band gap, and $n$ is the fitted exponent. For $E < E_G$, $I$ is set to 0. The fitting range was 1.5−3.5 eV. The fitting results are shown in Figure 5c. The analysis shows that the band gap ($E_G$) of violet-$P_{11}$ is around 2.1 ± 0.1 eV, which agrees with UV−Vis results. We note that for flake thicknesses ranging from 9 to 31 nm (0.2−0.69 inelastic mean free paths), the value of $E_G$ is essentially constant, which suggests that our analysis is not influenced by Cherenkov radiation or surface effects. The experimental results agree well with our DFT calculation results (vide infra). The UV−Vis spectrum and EELS analysis coupled with DFT calculation demonstrate the large band gap nature of violet-$P_{11}$.

**DFT Calculations.** Electronic band structures of both bulk violet-$P_{11}$ and single-layer violet-$P_{11}$ are obtained by DFT calculations, which are shown in Figure 6. The bulk violet-$P_{11}$ is computed to be a direct band gap semiconductor with a band gap of 1.80 eV at the Γ point in the Brillouin zone. The calculated band gap of bulk violet-$P_{11}$ is much higher than those of the bulk violet-$P_{21}$ (1.42 eV),[52] fibrous-$P_{21}$ (1.60 eV),[47] and bulk black-P (0.3 eV).[23] The measured optical band gap of bulk violet-$P_{11}$ is 2.0(1) eV for direct allowed transition (Figure 5a). Based on DFT calculation and UV−Vis results, the bulk violet-$P_{11}$ should be a direct band gap semiconductor with band gap of 2.0(1) eV. This large band gap of bulk violet-$P_{11}$ sets a new record for the band gap of layered elemental materials,[17−25,81] which opens a window for next-generation electronics and optoelectronics. The monolayer violet-$P_{11}$ is


https://doi.org/10.1021/jacs.3c01766
J. Am. Chem. Soc. 2023, 145, 8218−8230

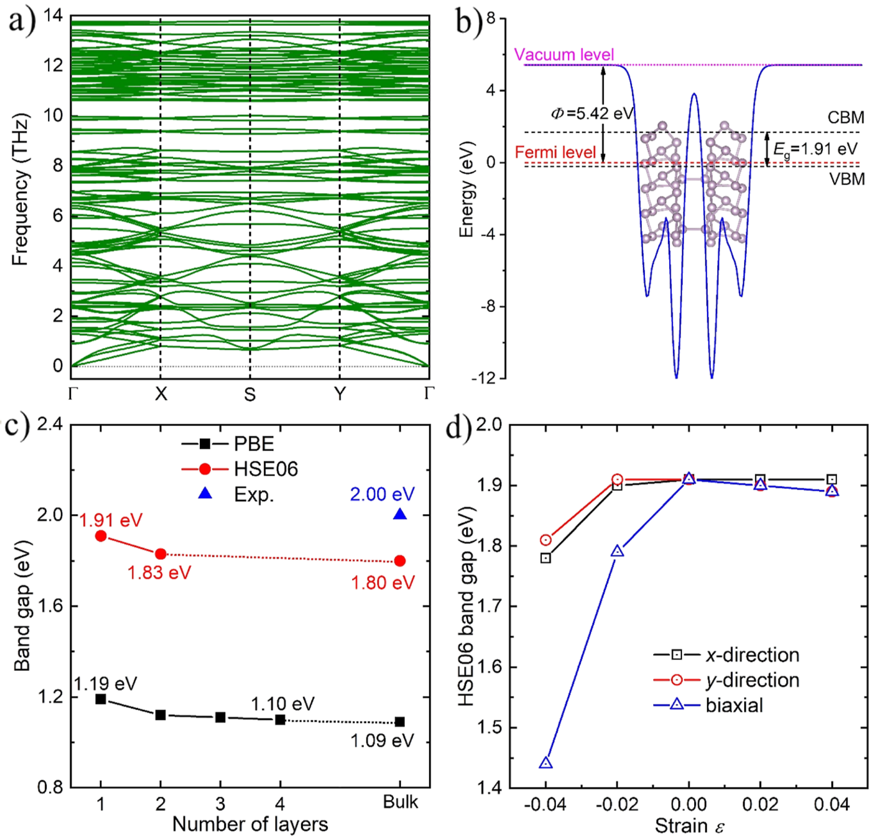


**Figure 7.** (a) Phonon spectrum of monolayer violet-$P_{11}$. (b) Electrostatic potentials and band edge alignments of monolayer violet-$P_{11}$. (c) Evolution of the calculated band gaps at the HSE06 and PBE levels as a function of the layer thickness of violet-$P_{11}$. The experimental band gap of bulk violet-$P_{11}$ is displayed for comparison. (d) HSE06 band gaps of monolayer violet-$P_{11}$ as a function of the in-plane uniaxial and biaxial strains, varying from −0.04 to 0.04.

predicted to be a direct semiconductor with a band gap of 1.91 eV at the Γ point. Interestingly, the band gap of monolayer violet-$P_{11}$ (1.91 eV) is comparable to that of bulk violet-$P_{11}$ (1.80 eV), whereas a significant difference exists between the band gaps of bulk and monolayer violet-$P_{21}$ (bulk: 1.42 eV and single layer: 2.54 eV)[52] and black-P (bulk: 0.3 eV and single layer: 1.9 eV).[23] Such large band gap discrepancy does not apply to the violet-$P_{11}$ and fibrous-$P_{21}$ (bulk: 1.60 eV and single layer: 1.69 eV).[47] The phosphorus allotropes exhibit very rich chemistry, which spans from 0D isolated [$P_4$] clusters in white phosphorus to 2D layered allotropes. Three 2D phosphorus allotropes were experimentally discovered prior to violet $P_{11}$: black P, violet-$P_{21}$, and fibrous-$P_{21}$. The violet-$P_{11}$ has the largest bulk band gap (2.0 eV) than other three phosphorus allotropes: black-P (0.3 eV),[23] violet-$P_{21}$ (1.42 eV),[52] and fibrous-$P_{21}$ (1.60 eV).[47]

To clarify the small difference between band gaps of bulk and monolayer of violet-$P_{11}$, additional calculations were employed to study the distribution of real-space wavefunction. The electron density distribution at the VBM and the CBM of bulk and monolayer violet-$P_{11}$ is shown in Figure 6, right. The electron density distributions of monolayer violet-$P_{11}$ are quite similar to those of bulk violet-$P_{11}$. The VBM is mainly dominated by the inner P atoms of the layer, while the CBM is mainly originated from the outer P atoms of the layer. The electrostatic potentials and band edge alignments of monolayer violet-$P_{11}$ were also calculated and are presented in Figure 7b. The VBM and CBM positions with vacuum level corrections are at −3.73 and −5.64 eV, respectively, and the calculated work function is 5.42 eV.

The phonon spectrum of monolayer violet-$P_{11}$ was calculated and is shown in Figure 7a. No appreciable negative frequency is found in the phonon spectrum, indicating that monolayer violet-$P_{11}$ is dynamically stable. The result of simulation agrees well with the experimental results. The thickness-dependent electronic structures of violet-$P_{11}$ were also studied (Figures 7c and S14). The electronic band structures of most multilayers of violet-$P_{11}$ were calculated at the PBE level and are shown in Figure S14. The calculated band gaps at the HSE06 and PBE levels as a function of the layer thickness (1L−4L) of violet-$P_{11}$ are shown in Figure 7c. Due to the small interlayer interaction and dispersion of the valence bands and the conduction bands, the band gap of violet-$P_{11}$ drops from 1.19 eV for the monolayer to 1.10 eV for the tetralayer, which is very close to a band gap of 1.09 eV for bulk. Actually, the layer-dependent trend of PBE band gaps is very similar to that of HSE06 band gaps. The HSE06 band gaps of monolayer and bilayer violet-$P_{11}$ are 1.91 and 1.83 eV, respectively, which is also close to that of bulk (1.80 eV). The potential impacts of stress on electronic structures of violet-$P_{11}$ were also studied via applying strains (Figures 7d and S15). The electronic structures of monolayer violet-$P_{11}$ under various applied uniaxial ($\varepsilon_{xx}$ and $\varepsilon_{yy}$) and biaxial ($\varepsilon_{xy}$) strains of −0.04 to 0.04 are investigated, as shown in Figure S15. The band gaps as a function of applied uniaxial and biaxial strains are shown in Figure 7d. The effect of tensile strains on the electronic structure of monolayer violet-$P_{11}$ is very small,


https://doi.org/10.1021/jacs.3c01766
J. Am. Chem. Soc. 2023, 145, 8218−8230

manifesting as almost unchanged energy band structure and band gap under small tensile strain (Figures 7d and S15). Please note that the electronic structure of monolayer violet-$P_{11}$ is relatively sensitive to compressive strain, especially biaxial strain. As shown in Figure S15, the location of CBM can shift from the Γ point to $S(Y)$ point under the uniaxial compressive strain $\varepsilon_{xx}$ ($\varepsilon_{yy}$) along the $x(y)$ direction, inducing the slight decrease of band gap. However, when applying the biaxial compressive strain on the monolayer violet-$P_{11}$, the location of CBM also moves from the Γ point to $Y$ point and exhibits the obvious downward shift. The band gap of monolayer violet-$P_{11}$ reduces to 1.44 eV under a biaxial compressive strain of −0.04.

The carrier mobilities of single-layer violet-$P_{11}$ are also calculated and summarized in Table 1. The single-layer violet-$P_{11}$ is predicted to have extraordinarily high carrier mobilities especially for electrons [$\mu_y$ = 1307.32 (cm$^2$ V$^{-1}$ s$^{-1}$)], although the FET measurements did not confirm the high mobility nature of violet-$P_{11}$ (*vide infra*). More detailed experiments are ongoing to investigate the carrier mobility of violet-$P_{11}$.

**Table 1. Calculated Carrier Mobility of Monolayer Violet-$P_{11}$**

| parameters | electrons | holes |
|---|---|---|
| $m_x^*/m_0$ | 0.25 | 0.35 |
| $m_y^*/m_0$ | 0.24 | 0.28 |
| $E_{1x}$ (eV) | 4.05 | 4.23 |
| $E_{1y}$ (eV) | 3.77 | 3.93 |
| $C_x^{2D}$ (N/m) | 51.82 | 51.82 |
| $C_y^{2D}$ (N/m) | 51.29 | 51.29 |
| $\mu_x$ (cm$^2$ V$^{-1}$ s$^{-1}$) | 1098.73 | 562.93 |
| $\mu_y$ (cm$^2$ V$^{-1}$s$^{-1}$) | 1307.32 | 806.85 |

**Violet-$P_{11}$-Based FET Attempts.** We fabricated an FET on an exfoliated violet-$P_{11}$ flake and back gated it to measure its transfer curve, as shown in Figure S16. The exfoliated flake has a thickness of 16.6 nm according to the AFM height trace in Figure S16c, corresponding to about eight units of phosphorus slabs. The back-gated transfer curve of this FET device obtained under ambient conditions in Figure S16d exhibits a typical n-type transport characteristic and suggests the dominant carrier in violet-$P_{11}$ at room temperature to be electrons. We further calculated the field-effect mobility of this device to be 6 × 10$^{-3}$ cm$^2$ V$^{-1}$ s$^{-1}$, which is far below the theoretically predicted value. Several intrinsic and extrinsic factors can contribute to this discrepancy between experimental data and theoretical prediction. (1) There exists a large Schottky barrier, approximately 1 eV difference between the metal work function of the contact metal Cr and violet-$P_{11}$'s electron affinity. A Schottky contact will severely degrade the device performance and lead to a significant underestimate of the electron mobility.[82] (2) The device fabrication process, such as electron beam lithography at 30 keV, might have brought electron knock-on damage in the flake and this will further lead to a worsened contact with the metal electrode. (3) The electrode deposition process through the e-beam evaporator might have locally heated the sample and thus resulted in unwanted irreversible thermal damage to the violet-$P_{11}$ flake. (4) Surface oxidation of the exfoliated flake during device fabrication would lead to degradation of mobility. Carrying out the fabrication process under an inert atmosphere or passivation of violet-$P_{11}$ is important for achieving high-quality devices and is ongoing. (5) Another worth mentioning point here is the possible overestimated theoretical carrier mobility by the deformation potentials (DP) theory, where the DP theory simply treats the scattering by longitudinal acoustic phonons and presumes the electron−phonon coupling to be isotropic.[83] A recent study of 2D $Ti_2CO_2$ MXenes demonstrated that the carrier mobility calculated by full electron−phonon coupling calculation is over 1 order of magnitude lower than that predicted by the traditional DP method.[83] To further study the carrier mobility of violet-$P_{11}$, more careful experimental studies such as fabricating devices in an inert atmosphere and theoretical studies such as fully considering electron−phonon coupling are important and ongoing.

As a new large band gap elemental 2D material, the violet-$P_{11}$ shows attractive properties. Electric properties of violet-$P_{11}$ and several 2D materials are compared in Table S7.[25,63,84−97] As shown in Table S7, the band gap of violet-$P_{11}$ is comparable to many promising 2D materials such as $MoS_2$,[84,85,87] $WS_2$,[25,86,88] and $Bi_2O_2Se$.[25,86,88,93,94] For theoretically predicted carrier mobility, violet-$P_{11}$ is close to $WS_2$[86,88] and higher than $MoS_2$,[84,85] $SnSe_2$,[86,88] $Bi_2O_2Se$,[94] and h-BN.[96,97] In addition, one advantage of violet-$P_{11}$ is its high ambient stability for bulk crystals. Another advantage of violet-$P_{11}$ is the easy growth as millimeter-sized crystals via a simple method, as shown in Figure S17. In contrast to conventional crystal growth methods of 2D materials such as chemical vapor deposition, molecular-beam epitaxy, and high-temperature solid-state methods, which are expensive and comprehensive, the crystal growth of violet-$P_{11}$ was carried out at moderately high temperature (773 K) with high yields. These millimeter-sized crystals were easily collected after a simple water wash (Figure S17), which makes future studies easy. The search for new 2D materials via theoretical studies and experiments is important and challenging.[98−101] The discovery of violet-$P_{11}$ showcases the rich chemistry of phosphorus allotropes and suggests the discovery of more novel 2D materials via facile chemistry synthesis methods possible. Due to the presence of free lone pairs, the ambient stability of thin flakes of phosphorus allotropes including violet-$P_{11}$ is moderate. Luckily, recent studies about passivation of black P were proved to be efficient,[26,102−104] which may guide the preparation of the device of violet-$P_{11}$.

## ■ CONCLUSIONS

A new 2D layered phosphorus allotrope, violet-$P_{11}$, was discovered by a high-temperature salt flux method. High quality and large yields of millimeter-sized violet-$P_{11}$ crystals, stable in water, were easily grown, which are crucial for future device fabrication. Violet-$P_{11}$ is also stable in ambient air after being exfoliated down to few layers for at least 1 h. PL emission spectra revealed the thickness-dependent nature and defect-dominant emission of violet-$P_{11}$. Violet-$P_{11}$ is a large band gap semiconductor of 2.0(1) eV, which is verified by UV−Vis spectra, EELS, and DFT calculations. DFT calculations predict that violet-$P_{11}$ is a direct band gap semiconductor with band gaps of 1.8 and 1.9 eV for bulk and monolayer, respectively, which agrees well with our experimental results. High carrier mobility is predicted for violet-$P_{11}$ by DFT calculations. The large band gap, facile growth of large crystals, excellent ambient stability for bulk crystals, and extraordinarily high predicted carrier mobility may indicate that violet-$P_{11}$ is a good candidate for next-generation electronics and optoelectronics.


https://doi.org/10.1021/jacs.3c01766
J. Am. Chem. Soc. 2023, 145, 8218−8230

## ASSOCIATED CONTENT

### Supporting Information

The Supporting Information is available free of charge at https://pubs.acs.org/doi/10.1021/jacs.3c01766.

> Refined crystallographic data, SEM images, EDS results, PXRD results, additional PL and Raman results, additional cross-sectional STEM, air exposure-dependent PL, HAADF STEM images, AFM results, optical micrographs, SEM images, addtional DFT calculation results, and crystal photos (PDF)

### Accession Codes

CCDC 2208167 contains the supplementary crystallographic data for this paper. These data can be obtained free of charge via www.ccdc.cam.ac.uk/data_request/cif, or by emailing data_request@ccdc.cam.ac.uk, or by contacting The Cambridge Crystallographic Data Centre, 12 Union Road, Cambridge CB2 1EZ, UK; fax: +44 1223 336033.

## AUTHOR INFORMATION

### Corresponding Authors

**Huabing Yin** − *Institute for Computational Materials Science, Joint Center for Theoretical Physics, and International Joint Research Laboratory of New Energy Materials and Devices of Henan Province, School of Physics and Electronics, Henan University, Kaifeng 475004, China;* orcid.org/0000-0001-5250-2430; Email: yhb@henu.edu.cn

**Judy J. Cha** − *Department of Mechanical Engineering and Materials Science, Yale University, New Haven, Connecticut 06520, United States; Department of Materials Science and Engineering, Cornell University, Ithaca, New York 14850, United States;* Email: jc476@cornell.edu

**Jian Wang** − *Department of Chemistry and Biochemistry, Wichita State University, Wichita, Kansas 67260, United States;* orcid.org/0000-0003-1326-4470; Email: jian.wang@wichita.edu

### Authors

**Gary Cicirello** − *Department of Chemistry and Biochemistry, Wichita State University, Wichita, Kansas 67260, United States*

**Mengjing Wang** − *Department of Mechanical Engineering and Materials Science, Yale University, New Haven, Connecticut 06520, United States; Department of Materials Science and Engineering, Cornell University, Ithaca, New York 14850, United States*

**Quynh P. Sam** − *Department of Materials Science and Engineering, Cornell University, Ithaca, New York 14850, United States*

**James L. Hart** − *Department of Materials Science and Engineering, Cornell University, Ithaca, New York 14850, United States*

**Natalie L. Williams** − *Department of Materials Science and Engineering, Cornell University, Ithaca, New York 14850, United States*

Complete contact information is available at: https://pubs.acs.org/10.1021/jacs.3c01766

### Author Contributions

[#]G.C. and M.W. are equally contributed.

### Notes

The authors declare no competing financial interest.

## ACKNOWLEDGMENTS

J.W. would like to thank Shannon Lee at Iowa State University for the help with EDX measurements. This research is supported by start-up funds from Wichita State University. M.W. is supported by Betty and Gordon Moore Foundation EPiQS Synthesis Investigator Award. Use of the Advanced Photon Source, an Office of Science User Facility operated for the U.S. Department of Energy (DOE) Office of Science by Argonne National Laboratory, was supported by the U.S. DOE under Contract no. DE-AC02-06CH11357. AFM was performed in part at the Cornell NanoScale Facility, a member of the National Nanotechnology Coordinated Infrastructure (NNCI), which is supported by the National Science Foundation (grant NNCI-2025233). Raman and SEM characterizations were performed at the Cornell Center for Materials Research Facilities supported by the National Science Foundation under Award Number DMR-1719875. This work made use of the electron microscopy facility of the Platform for the Accelerated Realization, Analysis, and Discovery of Interface Materials (PARADIM), which is supported by the National Science Foundation under Cooperative Agreement no. DMR-2039380. The FEI Titan Themis 300 was acquired through NSF-MRI-1429155, with additional support from Cornell University, the Weill Institute, and the Kavli Institute at Cornell.

## REFERENCES

(1) Novoselov, K. S.; Mishchenko, A.; Carvalho, A.; Castro Neto, A. H. 2D Materials and van Der Waals Heterostructures. *Science* **2016**, *353*, aac9439.

(2) Song, S.; Yoon, A.; Ha, J.-K.; Yang, J.; Jang, S.; Leblanc, C.; Wang, J.; Sim, Y.; Jariwala, D.; Min, S. K.; Lee, Z.; Kwon, S.-Y. Atomic Transistors Based on Seamless Lateral Metal-Semiconductor Junctions with a Sub-1-Nm Transfer Length. *Nat. Commun.* **2022**, *13*, 4916.

(3) Liu, G.; Tian, Z.; Yang, Z.; Xue, Z.; Zhang, M.; Hu, X.; Wang, Y.; Yang, Y.; Chu, P. K.; Mei, Y.; Liao, L.; Hu, W.; Di, Z. Graphene-Assisted Metal Transfer Printing for Wafer-Scale Integration of Metal Electrodes and Two-Dimensional Materials. *Nat. Electron.* **2022**, *5*, 275−280.

(4) Gao, X.; Vaidya, S.; Li, K.; Ju, P.; Jiang, B.; Xu, Z.; Allcca, A. E. L.; Shen, K.; Taniguchi, T.; Watanabe, K.; Bhave, S. A.; Chen, Y. P.; Ping, Y.; Li, T. Nuclear Spin Polarization and Control in Hexagonal Boron Nitride. *Nat. Mater.* **2022**, *21*, 1024−1028.

(5) Tsen, A. W.; Hunt, B.; Kim, Y. D.; Yuan, Z. J.; Jia, S.; Cava, R. J.; Hone, J.; Kim, P.; Dean, C. R.; Pasupathy, A. N. Nature of the Quantum Metal in a Two-Dimensional Crystalline Superconductor. *Nat. Phys.* **2016**, *12*, 208−212.

(6) Bae, S.; Matsumoto, K.; Raebiger, H.; Shudo, K. i.; Kim, Y.-H.; Handegård, Ø. S.; Nagao, T.; Kitajima, M.; Sakai, Y.; Zhang, X.; Vajtai, R.; Ajayan, P.; Kono, J.; Takeda, J.; Katayama, I. K-Point Longitudinal Acoustic Phonons Are Responsible for Ultrafast Intervalley Scattering in Monolayer $MoSe_2$. *Nat. Commun.* **2022**, *13*, 4279.

(7) Rho, Y.; Lee, K.; Wang, L.; Ko, C.; Chen, Y.; Ci, P.; Pei, J.; Zettl, A.; Wu, J.; Grigoropoulos, C. P. A Laser-Assisted Chlorination Process for Reversible Writing of Doping Patterns in Graphene. *Nat. Electron.* **2022**, *5*, 505−510.

(8) Bhimanapati, G. R.; Lin, Z.; Meunier, V.; Jung, Y.; Cha, J.; Das, S.; Xiao, D.; Son, Y.; Strano, M. S.; Cooper, V. R.; Liang, L.; Louie, S. G.; Ringe, E.; Zhou, W.; Kim, S. S.; Naik, R. R.; Sumpter, B. G.; Terrones, H.; Xia, F.; Wang, Y.; Zhu, J.; Akinwande, D.; Alem, N.; Schuller, J. A.; Schaak, R. E.; Terrones, M.; Robinson, J. A. Recent Advances in Two-Dimensional Materials beyond Graphene. *ACS Nano* **2015**, *9*, 11509−11539.

(9) Zeng, M.; Xiao, Y.; Liu, J.; Yang, K.; Fu, L. Exploring Two-Dimensional Materials toward the Next-Generation Circuits: From Monomer Design to Assembly Control. *Chem. Rev.* **2018**, *118*, 6236−6296.
(10) Mas-Ballesté, R.; Gómez-Navarro, C.; Gómez-Herrero, J.; Zamora, F. 2D Materials: To Graphene and Beyond. *Nanoscale* **2011**, *3*, 20−30.
(11) Ryu, B.; Wang, L.; Pu, H.; Chan, M. K. Y.; Chen, J. Understanding, Discovery, and Synthesis of 2D Materials Enabled by Machine Learning. *Chem. Soc. Rev.* **2022**, *51*, 1899−1925.
(12) Schneemann, A.; Dong, R.; Schwotzer, F.; Zhong, H.; Senkovska, I.; Feng, X.; Kaskel, S. 2D Framework Materials for Energy Applications. *Chem. Sci.* **2021**, *12*, 1600−1619.
(13) Montes-García, V.; Samorì, P. 2D Materials via Asymmetric Molecular Functionalization. *Chem. Sci.* **2022**, *13*, 315−328.
(14) Petocchi, F.; Nicholson, C. W.; Salzmann, B.; Pasquier, D.; Yazyev, O. V.; Monney, C.; Werner, P. Mott versus Hybridization Gap in the Low-Temperature Phase of 1T−$TaS_2$. *Phys. Rev. Lett.* **2022**, *129*, 016402.
(15) Achari, A.; Bekaert, J.; Sreepal, V.; Orekhov, A.; Kumaravadivel, P.; Kim, M.; Gauquelin, N.; Balakrishna Pillai, P.; Verbeeck, J.; Peeters, F. M.; Geim, A. K.; Milošević, M. V.; Nair, R. R. Alternating Superconducting and Charge Density Wave Monolayers within Bulk 6R-$TaS_2$. *Nano Lett.* **2022**, *22*, 6268−6275.
(16) Majed, A.; Kothakonda, M.; Wang, F.; Tseng, E. N.; Prenger, K.; Zhang, X.; Persson, P. O. Å.; Wei, J.; Sun, J.; Naguib, M. Transition Metal Carbo-Chalcogenide "TMCC:" A New Family of 2D Materials. *Adv. Mater.* **2022**, *34*, 2200574.
(17) Mannix, A. J.; Kiraly, B.; Hersam, M. C.; Guisinger, N. P. Synthesis and Chemistry of Elemental 2D Materials. *Nat. Rev. Chem.* **2017**, *1*, 0014.
(18) Xie, Z.; Zhang, B.; Ge, Y.; Zhu, Y.; Nie, G.; Song, Y.; Lim, C.-K.; Zhang, H.; Prasad, P. N. Chemistry, Functionalization, and Applications of Recent Monoelemental Two-Dimensional Materials and Their Heterostructures. *Chem. Rev.* **2022**, *122*, 1127−1207.
(19) Zhang, Y.; Rubio, A.; Lay, G. L. Emergent Elemental Two-Dimensional Materials beyond Graphene. *J. Phys. D: Appl. Phys.* **2017**, *50*, 053004.
(20) Fan, F. R.; Wang, R.; Zhang, H.; Wu, W. Emerging Beyond-Graphene Elemental 2D Materials for Energy and Catalysis Applications. *Chem. Soc. Rev.* **2021**, *50*, 10983−11031.
(21) Glavin, N. R.; Rao, R.; Varshney, V.; Bianco, E.; Apte, A.; Roy, A.; Ringe, E.; Ajayan, P. M. Emerging Applications of Elemental 2D Materials. *Adv. Mater.* **2020**, *32*, 1904302.
(22) Morpurgo, A. F. The ABC of 2D Materials. *Nat. Phys.* **2015**, *11*, 625−626.
(23) Castellanos-Gomez, A. Black Phosphorus: Narrow Gap, Wide Applications. *J. Phys. Chem. Lett.* **2015**, *6*, 4280−4291.
(24) Woods-Robinson, R.; Han, Y.; Zhang, H.; Ablekim, T.; Khan, I.; Persson, K. A.; Zakutayev, A. Wide Band Gap Chalcogenide Semiconductors. *Chem. Rev.* **2020**, *120*, 4007−4055.
(25) Chaves, A.; Azadani, J. G.; Alsalman, H.; da Costa, D. R.; Frisenda, R.; Chaves, A. J.; Song, S. H.; Kim, Y. D.; He, D.; Zhou, J.; Castellanos-Gomez, A.; Peeters, F. M.; Liu, Z.; Hinkle, C. L.; Oh, S.-H.; Ye, P. D.; Koester, S. J.; Lee, Y. H.; Avouris, Ph.; Wang, X.; Low, T. Bandgap Engineering of Two-Dimensional Semiconductor Materials. *npj 2D Mater. Appl.* **2020**, *4*, 29.
(26) Abate, Y.; Akinwande, D.; Gamage, S.; Wang, H.; Snure, M.; Poudel, N.; Cronin, S. B. Recent Progress on Stability and Passivation of Black Phosphorus. *Adv. Mater.* **2018**, *30*, 1704749.
(27) Marangoni, V. S.; Cadore, A. R.; Ribeiro, H. B.; Hostert, L.; de Matos, C. J. S.; Silva, C. C. C.; Seixas, L.; Maroneze, C. M. Long-Term Environmental Stability of Nitrogen-Healed Black Phosphorus. *Appl. Surf. Sci.* **2021**, *564*, 150450.
(28) Illarionov, Yu. Yu.; Waltl, M.; Rzepa, G.; Knobloch, T.; Kim, J.-S.; Akinwande, D.; Grasser, T. Highly-Stable Black Phosphorus Field-Effect Transistors with Low Density of Oxide Traps. *npj 2D Mater. Appl.* **2017**, *1*, 23.
(29) Illarionov, Y. Y.; Waltl, M.; Rzepa, G.; Kim, J.-S.; Kim, S.; Dodabalapur, A.; Akinwande, D.; Grasser, T. Long-Term Stability and Reliability of Black Phosphorus Field-Effect Transistors. *ACS Nano* **2016**, *10*, 9543−9549.
(30) Liu, X.; Xiao, L.; Weng, J.; Xu, Q.; Li, W.; Zhao, C.; Xu, J.; Zhao, Y. Regulating the Reactivity of Black Phosphorus via Protective Chemistry. *Sci. Adv.* **2020**, *6*, No. eabb4359.
(31) Wan, D.; Huang, H.; Wang, Z.; Liu, X.; Liao, L. Recent Advances in Long-Term Stable Black Phosphorus Transistors. *Nanoscale* **2020**, *12*, 20089−20099.
(32) Kou, L.; Chen, C.; Smith, S. C. Phosphorene: Fabrication, Properties, and Applications. *J. Phys. Chem. Lett.* **2015**, *6*, 2794−2805.
(33) *Fundamentals and Applications of Phosphorus Nanomaterials*; Ji, H.-F., Ed.; ACS Symposium Series; American Chemical Society: Washington, DC, 2019; Vol. 1333
(34) Gusmão, R.; Sofer, Z.; Pumera, M. Black Phosphorus Rediscovered: From Bulk Material to Monolayers. *Angew. Chem., Int. Ed.* **2017**, *56*, 8052−8072.
(35) Ruck, M.; Hoppe, D.; Wahl, B.; Simon, P.; Wang, Y.; Seifert, G. Fibrous Red Phosphorus. *Angew. Chem., Int. Ed.* **2005**, *44*, 7616−7619.
(36) Liu, J.; Zhang, S.; Guo, Y.; Wang, Q. Phosphorus K4 Crystal: A New Stable Allotrope. *Sci. Rep.* **2016**, *6*, 37528.
(37) Li, Z.; He, C.; Ouyang, T.; Zhang, C.; Tang, C.; Römer, R. A.; Zhong, J. Allotropes of Phosphorus with Remarkable Stability and Intrinsic Piezoelectricity. *Phys. Rev. Appl.* **2018**, *9*, 044032.
(38) Zhuo, Z.; Wu, X.; Yang, J. Three-Dimensional Covalently Linked Allotropic Structures of Phosphorus. *J. Phys. Chem. C* **2016**, *120*, 26453−26458.
(39) Liu, J.; Guo, Y.; Zhang, S.; Wang, Q.; Kawazoe, Y.; Jena, P. New Phosphorene Allotropes Containing Ridges with 2- and 4-Coordination. *J. Phys. Chem. C* **2015**, *119*, 24674−24680.
(40) Le, M.-Q. Reactive Molecular Dynamics Simulations of the Mechanical Properties of Various Phosphorene Allotropes. *Nanotechnology* **2018**, *29*, 195701.
(41) Demingos, P. G.; Muniz, A. R. Prediction of $\phi$-P and $\sigma$-P: Two New Strain-Interconvertible Phosphorene Allotropes. *J. Phys. Chem. C* **2020**, *124*, 21207−21214.
(42) Aykol, M.; Doak, J. W.; Wolverton, C. Phosphorus Allotropes: Stability of Black versus Red Phosphorus Re-Examined by Means of the van Der Waals Inclusive Density Functional Method. *Phys. Rev. B* **2017**, *95*, 214115.
(43) Pfitzner, A. Phosphorus Remains Exciting. *Angew. Chem., Int. Ed.* **2006**, *45*, 699−700.
(44) Pfitzner, A.; Bräu, M. F.; Zweck, J.; Brunklaus, G.; Eckert, H. Phosphorus Nanorods—Two Allotropic Modifications of a Long-Known Element. *Angew. Chem., Int. Ed.* **2004**, *43*, 4228−4231.
(45) Bachhuber, F.; von Appen, J.; Dronskowski, R.; Schmidt, P.; Nilges, T.; Pfitzner, A.; Weihrich, R. The Extended Stability Range of Phosphorus Allotropes. *Angew. Chem., Int. Ed.* **2014**, *53*, 11629−11633.
(46) Hittorf, W. Zur Kenntniss des Phosphors. *Ann. Chem. Phys.* **1865**, *202*, 193−228.
(47) Sun, Z.; Zhang, B.; Zhao, Y.; Khurram, M.; Yan, Q. Synthesis, Exfoliation, and Transport Properties of Quasi-1D van Der Waals Fibrous Red Phosphorus. *Chem. Mater.* **2021**, *33*, 6240−6248.
(48) Zhao, Y.; Sun, Z.; Zhang, B.; Yan, Q. Unveiling the Degradation Chemistry of Fibrous Red Phosphorus under Ambient Conditions. *ACS Appl. Mater. Interfaces* **2022**, *14*, 9925−9932.
(49) Ricciardulli, A. G.; Wang, Y.; Yang, S.; Samorì, P. Two-Dimensional Violet Phosphorus: A p-Type Semiconductor for (Opto)Electronics. *J. Am. Chem. Soc.* **2022**, *144*, 3660−3666.
(50) Zhang, W.; Enriquez, H.; Tong, Y.; Mayne, A. J.; Bendounan, A.; Smogunov, A.; Dappe, Y. J.; Kara, A.; Dujardin, G.; Oughaddou, H. Flat Epitaxial Quasi-1D Phosphorene Chains. *Nat. Commun.* **2021**, *12*, 5160.
(51) Amaral, P. E. M.; Hall, D. C.; Pai, R.; Król, J. E.; Kalra, V.; Ehrlich, G. D.; Ji, H.-F. Fibrous Phosphorus Quantum Dots for Cell Imaging. *ACS Appl. Nano Mater.* **2020**, *3*, 752−759.

(52) Zhang, L.; Huang, H.; Zhang, B.; Gu, M.; Zhao, D.; Zhao, X.; Li, L.; Zhou, J.; Wu, K.; Cheng, Y.; Zhang, J. Structure and Properties of Violet Phosphorus and Its Phosphorene Exfoliation. *Angew. Chem., Int. Ed.* **2020**, *59*, 1074−1080.
(53) Kresse, G.; Furthmüller, J. Efficient Iterative Schemes for Ab Initio Total-Energy Calculations Using a Plane-Wave Basis Set. *Phys. Rev. B: Condens. Matter Mater. Phys.* **1996**, *54*, 11169−11186.
(54) Kresse, G.; Furthmüller, J. Efficiency of Ab-Initio Total Energy Calculations for Metals and Semiconductors Using a Plane-Wave Basis Set. *Comput. Mater. Sci.* **1996**, *6*, 15−50.
(55) Kresse, G.; Joubert, D. From Ultrasoft Pseudopotentials to the Projector Augmented-Wave Method. *Phys. Rev. B: Condens. Matter Mater. Phys.* **1999**, *59*, 1758−1775.
(56) Perdew, J. P.; Burke, K.; Ernzerhof, M. Generalized Gradient Approximation Made Simple. *Phys. Rev. Lett.* **1996**, *77*, 3865−3868.
(57) Monkhorst, H. J.; Pack, J. D. Special Points for Brillouin-Zone Integrations. *Phys. Rev. B: Condens. Matter Mater. Phys.* **1976**, *13*, 5188−5192.
(58) Grimme, S.; Antony, J.; Ehrlich, S.; Krieg, H. A Consistent and Accurate Ab Initio Parametrization of Density Functional Dispersion Correction (DFT-D) for the 94 Elements H-Pu. *J. Chem. Phys.* **2010**, *132*, 154104.
(59) Heyd, J.; Scuseria, G. E.; Ernzerhof, M. Hybrid Functionals Based on a Screened Coulomb Potential. *J. Chem. Phys.* **2003**, *118*, 8207−8215.
(60) Togo, A.; Tanaka, I. First principles phonon calculations in materials science. *Scr. Mater.* **2015**, *108*, 1−5.
(61) Nosé, S. A unified formulation of the constant temperature molecular dynamics methods. *J. Chem. Phys.* **1984**, *81*, 511.
(62) Hoover, W. G. Canonical dynamics: Equilibrium phase-space distributions. *Phys. Rev. A* **1985**, *31*, 1695.
(63) Bardeen, J.; Shockley, W. Deformation Potentials and Mobilities in Non-Polar Crystals. *Phys. Rev.* **1950**, *80*, 72−80.
(64) Jiang, S.; Li, J.; Chen, W.; Yin, H.; Zheng, G.-P.; Wang, Y. InTeI. InTeI: a novel wide-bandgap 2D material with desirable stability and highly anisotropic carrier mobility. *Nanoscale* **2020**, *12*, 5888−5897.
(65) Chen, W.; Yin, H.; Jiang, S.; Liu, S.; Liu, C.; Wang, B.; Zheng, G.-P. Anomalous Layer-Dependent Electronic and Piezoelectric Properties of 2D $GaInS_3$ Nanosheets. *Appl. Phys. Lett.* **2021**, *118*, 213103.
(66) Qiao, J.; Kong, X.; Hu, Z.-X.; Yang, F.; Ji, W. High-Mobility Transport Anisotropy and Linear Dichroism in Few-Layer Black Phosphorus. *Nat. Commun.* **2014**, *5*, 4475.
(67) Wang, J.; Yox, P.; Voyles, J.; Kovnir, K. Synthesis, Crystal Structure, and Properties of Three La−Zn−P Compounds with Different Dimensionalities of the Zn−P Framework. *Cryst. Growth Des.* **2018**, *18*, 4076−4083.
(68) Bridgman, P. W. Two New Modifications of Phosphorus. *J. Am. Chem. Soc.* **1914**, *36*, 1344−1363.
(69) Wang, J.; He, Y.; Mordvinova, N. E.; Lebedev, O. I.; Kovnir, K. The Smaller the Better: Hosting Trivalent Rare-Earth Guests in Cu−P Clathrate Cages. *Chem* **2018**, *4*, 1465−1475.
(70) Nguyen, V.; Ji, B.; Wu, K.; Zhang, B.; Wang, J. Unprecedented Mid-Infrared Nonlinear Optical Materials Achieved by Crystal Structure Engineering, a Case Study of $(KX)P_2S_6$ (X = Sb, Bi, Ba). *Chem. Sci.* **2022**, *13*, 2640−2648.
(71) Wang, J.; Voyles, J.; Grzybowski, S.; Kovnir, K. Structure, and Transport Properties of $Ba_8Cu_{16-x}Au_xP_{30}$ Clathrate Solid Solution. *J. Appl. Phys.* **2020**, *127*, 055104.
(72) Wang, J.; Lee, K.; Kovnir, K. Crystal Structure, and Properties of $La_4Zn_7P_{10}$ and $La_4Mg_{1.5}Zn_{8.5}P_{12}$. *Inorg. Chem.* **2017**, *56*, 783−790.
(73) Fasol, G.; Cardona, M.; Hönle, W.; von Schnering, H. G. Lattice Dynamics of Hittorf's Phosphorus and Identification of Structural Groups and Defects in Amorphous Red Phosphorus. *Solid State Commun.* **1984**, *52*, 307−310.
(74) Pelant, I.; Valenta, J. *Luminescence Spectroscopy of Semiconductors*; Oxford University Press, 2012.
(75) Wu, K.; Zhong, H.; Guo, Q.; Tang, J.; Yang, Z.; Qian, L.; Yuan, S.; Zhang, S.; Xu, H. Revealing the Competition between Defect-Trapped Exciton and Band-Edge Exciton Photoluminescence in Monolayer Hexagonal $WS_2$. *Adv. Opt. Mater.* **2022**, *10*, 2101971.
(76) Castellanos-Gomez, A.; Vicarelli, L.; Prada, E.; Island, J. O.; Narasimha-Acharya, K. L.; Blanter, S. I.; Groenendijk, D. J.; Buscema, M.; Steele, G. A.; Alvarez, J. V.; Zandbergen, H. W.; Palacios, J. J.; van der Zant, H. S. J. Isolation and Characterization of Few-Layer Black Phosphorus. *2D Mater.* **2014**, *1*, 025001.
(77) Hanlon, D.; Backes, C.; Doherty, E.; Cucinotta, C. S.; Berner, N. C.; Boland, C.; Lee, K.; Harvey, A.; Lynch, P.; Gholamvand, Z.; Zhang, S.; Wang, K.; Moynihan, G.; Pokle, A.; Ramasse, Q. M.; McEvoy, N.; Blau, W. J.; Wang, J.; Abellan, G.; Hauke, F.; Hirsch, A.; Sanvito, S.; O'Regan, D. D.; Duesberg, G. S.; Nicolosi, V.; et al. Liquid Exfoliation of Solvent-Stabilized Few-Layer Black Phosphorus for Applications Beyond Electronics. *Nat. Commun.* **2015**, *6*, 8563.
(78) Pei, J. J.; Gai, X.; Yang, J.; Wang, X. B.; Yu, Z. F.; Choi, D. Y.; Luther-Davies, B.; Lu, Y. R. Producing air-stable monolayers of phosphorene and their defect engineering. *Nat. Commun.* **2016**, *7*, 10450.
(79) Guan, J.; Zhu, Z.; Tománek, D. Phase Coexistence and Metal−-Insulator Transition in Few-Layer Phosphorene: A Computational Study. *Phys. Rev. Lett.* **2014**, *113*, 046804.
(80) Wang, G.; Slough, W. J.; Pandey, R.; Karna, S. P. Degradation of Phosphorene in Air: Understanding at Atomic Level. *2D Mater.* **2016**, *3*, 025011.
(81) Lu, Y.; Warner, J. H. Synthesis and Applications of Wide Bandgap 2D Layered Semiconductors Reaching the Green and Blue Wavelengths. *ACS Appl. Electron. Mater.* **2020**, *2*, 1777−1814.
(82) Shen, P.-C.; Su, C.; Lin, Y.; Chou, A.-S.; Cheng, C.-C.; Park, J.-H.; Chiu, M.-H.; Lu, A.-Y.; Tang, H.-L.; Tavakoli, M. M.; Pitner, G.; Ji, X.; Cai, Z.; Mao, N.; Wang, J.; Tung, V.; Li, J.; Bokor, J.; Zettl, A.; Wu, C.-I.; et al. Ultralow Contact Resistance between Semimetal and Monolayer Semiconductors. *Nature* **2021**, *593*, 211−217.
(83) Peng, L.; Huang, Y.; Zhou, J.; Sun, Z. Polar Optical-Phonon Dominated Electrical Transport in Ti2CO2 MXene. *J. Phys. Chem. C* **2023**, *127*, 3349−3354.
(84) Restrepo, O. D.; Krymowski, K. E.; Goldberger, J.; Windl, W. A First Principles Method to Simulate Electron Mobilities in 2D Materials. *New J. Phys.* **2014**, *16*, 105009.
(85) Cheng, L.; Zhang, C.; Liu, Y. Why Two-Dimensional Semiconductors Generally Have Low Electron Mobility. *Phys. Rev. Lett.* **2020**, *125*, 177701.
(86) Liu, Y.; Duan, X.; Huang, Y.; Duan, X. Two-Dimensional Transistors beyond Graphene and TMDCs. *Chem. Soc. Rev.* **2018**, *47*, 6388−6409.
(87) Splendiani, A.; Sun, L.; Zhang, Y.; Li, T.; Kim, J.; Chim, C.-Y.; Galli, G.; Wang, F. Emerging Photoluminescence in Monolayer $MoS_2$. *Nano Lett.* **2010**, *10*, 1271−1275.
(88) Zhang, W.; Huang, Z.; Zhang, W.; Li, Y. Two-Dimensional Semiconductors with Possible High Room Temperature Mobility. *Nano Res.* **2014**, *7*, 1731−1737.
(89) Arora, H.; Erbe, A. Recent Progress in Contact, Mobility, and Encapsulation Engineering of InSe and GaSe. *InfoMat* **2021**, *3*, 662−693.
(90) Chen, J.; Tan, X.; Lin, P.; Sa, B.; Zhou, J.; Zhang, Y.; Wen, C.; Sun, Z. Comprehensive Understanding of Intrinsic Mobility in the Monolayers of III−VI Group 2D Materials. *Phys. Chem. Chem. Phys.* **2019**, *21*, 21898−21907.
(91) Shafique, A.; Samad, A.; Shin, Y.-H. Ultra Low Lattice Thermal Conductivity and High Carrier Mobility of Monolayer $SnS_2$ and $SnSe_2$: A First Principles Study. *Phys. Chem. Chem. Phys.* **2017**, *19*, 20677−20683.
(92) Guo, C.; Tian, Z.; Xiao, Y.; Mi, Q.; Xue, J. Field-Effect Transistors of High-Mobility Few-Layer $SnSe_2$. *Appl. Phys. Lett.* **2016**, *109*, 203104.
(93) Chen, C.; Wang, M.; Wu, J.; Fu, H.; Yang, H.; Tian, Z.; Tu, T.; Peng, H.; Sun, Y.; Xu, X.; Jiang, J.; Schröter, N. B. M.; Li, Y.; Pei, D.; Liu, S.; Ekahana, S. A.; Yuan, H.; Xue, J.; Li, G.; Jia, J.; Liu, Z.; Yan, B.;


https://doi.org/10.1021/jacs.3c01766
J. Am. Chem. Soc. 2023, 145, 8218−8230

Peng, H.; Chen, Y. Electronic Structures and Unusually Robust Bandgap in an Ultrahigh-Mobility Layered Oxide Semiconductor, Bi2O2Se. *Sci. Adv.* **2018**, *4*, No. eaat8355.
(94) Wang, N.; Li, M. L.; Xiao, H. Y.; Gong, H. F.; Liu, Z. J.; Zu, X. T.; Qiao, L. Optimizing the thermoelectric transport properties of $Bi_2O_2Se$ monolayer via biaxial strain. *Phys. Chem. Chem. Phys.* **2019**, *21*, 15097−15105.
(95) Sasama, Y.; Komatsu, K.; Moriyama, S.; Imura, M.; Teraji, T.; Watanabe, K.; Taniguchi, T.; Uchihashi, T.; Takahide, Y. High-Mobility Diamond Field Effect Transistor with a Monocrystalline h-BN Gate Dielectric. *APL Mater.* **2018**, *6*, 111105.
(96) Liu, L.; Feng, Y. P.; Shen, Z. X. Structural and Electronic Properties of h-BN. *Phys. Rev. B: Condens. Matter Mater. Phys.* **2003**, *68*, 104102.
(97) Khatami, M. M.; Van de Put, M. L.; Vandenberghe, W. G. First-Principles Study of Electronic Transport in Germanane and Hexagonal Boron Nitride. *Phys. Rev. B* **2021**, *104*, 235424.
(98) Duong, D. L.; Yun, S. J.; Lee, Y. H. van der Waals Layered Materials: Opportunities and Challenges. *ACS Nano* **2017**, *11*, 11803−11830.
(99) Gan, Y.; Miao, N.; Lan, P.; Zhou, J.; Elliott, S. R.; Sun, Z. Robust Design of High-Performance Optoelectronic Chalcogenide Crystals from High-Throughput Computation. *J. Am. Chem. Soc.* **2022**, *144*, 5878−5886.
(100) Zhang, T.; Wang, Y.; Li, H.; Zhong, F.; Shi, J.; Wu, M.; Sun, Z.; Shen, W.; Wei, B.; Hu, W.; Liu, X.; Huang, L.; Hu, C.; Wang, Z.; Jiang, C.; Yang, S.; Zhang, Q. m.; Qu, Z. Magnetism and Optical Anisotropy in van Der Waals Antiferromagnetic Insulator CrOCl. *ACS Nano* **2019**, *13*, 11353−11362.
(101) Zhang, Y.; Sa, B.; Miao, N.; Zhou, J.; Sun, Z. Computational Mining of Janus $Sc_2C$-Based MXenes for Spintronic, Photocatalytic, and Solar Cell Applications. *J. Mater. Chem. A* **2021**, *9*, 10882−10892.
(102) Ryder, C. R.; Wood, J. D.; Wells, S. A.; Yang, Y.; Jariwala, D.; Marks, T. J.; Schatz, G. C.; Hersam, M. C. Covalent Functionalization and Passivation of Exfoliated Black Phosphorus via Aryl Diazonium Chemistry. *Nat. Chem.* **2016**, *8*, 597−602.
(103) Gamage, S.; Li, Z.; Yakovlev, V. S.; Lewis, C.; Wang, H.; Cronin, S. B.; Abate, Y. Nanoscopy of Black Phosphorus Degradation. *Adv. Mater. Interfaces* **2016**, *3*, 1600121.
(104) Wood, J. D.; Wells, S. A.; Jariwala, D.; Chen, K.-S.; Cho, E.; Sangwan, V. K.; Liu, X.; Lauhon, L. J.; Marks, T. J.; Hersam, M. C. Effective Passivation of Exfoliated Black Phosphorus Transistors against Ambient Degradation. *Nano Lett.* **2014**, *14*, 6964−6970.




https://doi.org/10.1021/jacs.3c01766
*J. Am. Chem. Soc.* 2023, 145, 8218−8230